Electronically controlled optical beam-steering by an active phased array of metallic nanoantennas

C. T. DeRose,[1] **R. D. Kekatpure,**[1] **D. C. Trotter,**[1] **A. Starbuck,**[1] **J. R. Wendt,**[1] **A. Yaacobi,**[2] **M. R. Watts,**[2] **U. Chettiar,**[3] **N. Engheta,**[3] **and P. S. Davids**[1*]

[1] *Sandia National Laboratories,*
PO Box 5800 Albuquerque, NM 87185 USA
[2] *Research Laboratory of Electronics,*
Massachusetts Institute of Technology, Cambridge, MA 02139 USA
[3] *Department of Electrical and Systems Engineering,*
University of Pennsylvania,Philadelphia, PA 19104-6314 USA

*[*]*pdavids@sandia.gov*

Abstract: An optical phased array of nanoantenna fabricated in a CMOS compatible silicon photonics process is presented. The optical phased array is fed by low loss silicon waveguides with integrated ohmic thermo-optic phase shifters capable of 2π phase shift with ~ 15 mW of applied electrical power. By controlling the electrical power to the individual integrated phase shifters fixed wavelength steering of the beam emitted normal the surface of the wafer of $8°$ is demonstrated for 1×8 phased arrays with periods of both 6 and 9 μm.

OCIS codes: (230.0230) Optical devices; (240.3990) Micro-optical devices; (240.6690) Surface waves; (050.1960) Diffraction theory; (050.1220) Apertures.

References and links

1. T. K. Sarkar, M. C. Wicks, S.-P. Magdalena, and R. J. Bonneau, *Smart Antennas* (John Wiley & Sons, Inc., 2000).
2. B. D. Steinberg, *Microwave imaging with large antenna arrays: Radio Camera Principles and Techniques* (Wiley-Interscience, 1983).
3. S. Young and B. Schwarz, "LIDAR in the drivers seat," Optics and Photonics **12** (March) (2010).
4. B. Schwarz, "Lidar: Mapping the world in 3D," Nat. Photonics, **4**(7), 429–430 (2010).
5. L. Novotny and N. van Hulst, "Antennas for light," Nat. Photonics, **5**(2), 83–90 (2011).
6. M. Schnell, A. Garcia-Etxarri, A. J. Huber, K. Crozier, J. Aizpurua, and R. Hillenbrand, "Controlling the near-field oscillations of loaded plasmonic nanoantennas," Nature (London) **3**(April), 287–291 (2009).
7. W. Cai, C. Jun, and J. White, "Plasmonics for extreme light concentration and manipulation," Nature (London) **9**(3), 193–204 (2010).
8. W. Zhou and T. W. Odom, "Tunable subradiant lattice plasmons by out-of-plane dipolar interactions," Nature Nanotechnology **6**(7), 423–7 (2011).
9. A. Alù and N. Engheta, "Tuning the scattering response of optical nanoantennas with nanocircuit loads," Nat. Photonics **2**(5), 307–310 (2008).
10. D. de Ceglia, M. A. Vincenti, and M. Scalora, "Wideband plasmonic beam steering in metal gratings," Opt. Lett. **37**(2), 271 (2012).
11. E. S. Barnard, R. A. Pala, and M. L. Brongersma, "Photocurrent mapping of near-field optical antenna resonances," Nature Nanotechnology **6**(9), 588–93 (2011).
12. K. Van Acoleyen, H. Rogier, and R. Baets, "Two-dimensional optical phased array antenna on silicon-on-insulator," Opt. Express **18**(13), 13655–13660 (2010).
13. J. K. Doylend, M. J. R. Heck, J. T. Bovington, J. D. Peters, L. A. Coldren, and J. E. Bowers, "Two-dimensional free-space beam steering with an optical phased array on silicon-on-insulator," Opt. Express **19**(22), 21595–21604 (2011).

14. J. Sun, E. Timurdogan, A. Yaacobi, E. Shah Hosseini, D. Coolbaugh, and M. R. Watts, "Large-scale nanophotonic phased array ," Nature (London) , **493**, 195-199 (2013).
15. A. Yaacobi, E. Timurdogan, and M. Watts, "Vertical emitting aperture nanoantennas," Opt. Lett. **37**, 1454-1456 (2012).
16. J. D. Jackson, *Classical Electrodynamics*, 2nd ed. (John Wiley & Sons, Inc., 1975).
17. G. Cocorullo, F. G. Della Corte, and I. Rendina, "Temperature dependence of the thermo-optic coefficient in crystalline silicon between room temperature and 550 K at the wavelength of 1523 nm," Appl. Phys. Lett. **74**(22), 3338 (1999).
18. M. R. Watts,"Adiabatic microring resonators," Opt. Lett. **35**, 3231–3233 (2010).
19. C. T. Derose, D. C. Trotter, W. A. Zortman, A. L. Starbuck, M. Fisher, M. R. Watts, and P. S. Davids, "Ultra compact 45 GHz CMOS compatible germanium waveguide photodiode with low dark current," Opt. Express **19**(25), 527–534 (2011).

1. Introduction

Radio frequency and microwave phased arrays have been used extensively for a large host of applications ranging from wireless base-stations [1] for mobile communications to radio astronomy [2]. They are typically phase coherent spatially separated arrays of antenna radiating elements with electronically controlled amplitudes and phases for beam-shaping and steering, respectively. Here we present the first demonstration of an active chip-scale optical phased array based on metallic nanoantenna emitters operating in the near-infrared. Our nanoantenna emitters are fed by low loss silicon waveguides and individually phase controlled to radiate and steer a surface normal beam. In our CMOS compatible optical phased array architecture, we actively control the phase of each radiating nanoantenna by utilizing compact Silicon photonic phase-shifters integrated directly into our waveguides, and have demonstrated wide angle optical beam-steering at fixed wavelength.

An optical chip-scale electronic beam-steering device would greatly impact laser ranging and detection (LIDAR) and could enable handheld remote sensing and imaging devices for geographic information systems (GIS) [3, 4]. By removing large bulky mechanical parts, such as gimbals, mirrors, and motors, compact chip-scale electronically controlled beam-steering can considerably reduce size, weight, and power requirements and enable many new applications; like robotic vehicle sensors and peer-to-peer free-space communication links. Furthermore, a frequency agile optical phased array would be extremely desirable for high bandwidth free-space peer-to-peer communication links. A key element of this technology is a compact, electronically tuned wide-angle optical beam-steering device based on our Silicon photonics phased-array architecture with our newly integrated metallic nanoantenna operating in the near-infrared wavelength bands.

Passive metallic nanoantenna and nanoantenna arrays have been extensively investigated in the optical domain for field concentration and enhanced non-linearity for sensing [5–9]. New theoretical [9,10] and experimental techniques [11] have been developed to examine plasmonic resonances in these passive nanoantenna structures. Recently, active chip-scale optical phased array beam-steering devices based on gratings have been demonstrated [12, 13]. These grating approaches use wavelength tuning to steer the beam along one axis and various electronically controlled phase modulators for steering along the orthogonal axis. These devices have good 2D steering performance, but due to the wavelength tuning are undesirable for free-space communication links since they cannot operate at fixed wavelength or point in a fixed direction and vary wavelength. The ability to simultaneously point and to scan wavelength is a requirement for most free-space communication and sensing applications. Recently, a large-scale thermo-optically tunable phase array of dielectric grating elements has been demonstrated where the phase shifters embedded in each unit cell were coded in a digital way to realize 2D optical beam steering [14]. In this paper, we demonstrate an alternative approach using metallic nanoantenna phased arrays where the beam can be continuously angularly steered. Metallic antennas can be

compact, efficient radiators [15] due to the high dielectric permittivity contrast between metals and the cladding dielectric materials. They are scalable to optical frequencies where resonant surface excitations can be exploited to enhance their radiative properties. In contrast, dielectric antenna arrays offer lower absorption losses but are limited in the dielectric contrast that can be obtained in the restricted subset of CMOS compatible materials.
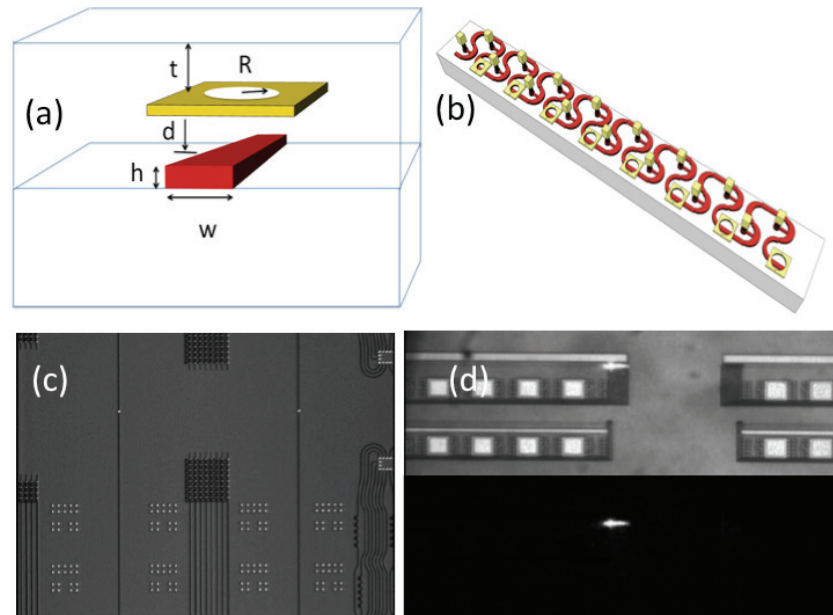

Fig. 1. (a) Schematic of the waveguide fed circular aperture antenna. (b) Schematic view of 1×8 linear antenna array with integrated thermo-optic phase shifter. The antenna are variable circular apertures in thin metallic sheets. $R_1 = 500$ nm, $R_2 = 550$ nm, $R_3 = 650$ nm, and $R = 750$nm for the remaining apertures. (c) SEM image of chip-scale arrays after metal antenna patterning. (d) Real-space image of light collected from waveguide fed linear antenna array. Upper image under near-IR diode illumination. Lower image in the dark.

Our approach to realize an electronically controlled optical beam-steering device is based on the principle of antenna phased arrays. Optical antennas differ from radio-frequency (RF) or microwave antenna because at high frequencies radiation reaction and damping effects are appreciable. Therefore, we cannot simply treat metals at optical frequencies as perfect conductors and need to design for material loss and dispersion and to treat non-ideality in the optical response of a metallic optical nanoantenna. Furthermore, there exists collective excitation of optical modes at metallic surfaces that can be used to tightly confine and guide light at metal dielectric surfaces. These guided surface modes are tightly confined to sub-wavelength dimensions and can be readily coupled into from a high index dielectric waveguide. Thus metallic antenna emitters are highly tailorable based on metal geometry and can be designed to couple efficiently to free-space radiative modes making them ideal compact feed and antenna structures for optical fields. This leads us to consider a hybrid optical phased array architecture based on low-loss dielectric waveguides for the distribution and phase-modulation of the optical signal, and metallic nanoantenna structures above a properly placed ground plane as the radiating element [15].

2. Optical phased array

In an optical phased array, control of the individual emitting antenna elements amplitude and phase allows for the complete tailoring of the far-field beam profile. Here we demonstrate control of the optical phase with integrated optical phase shifters and amplitude control by apodization of the nanoantenna apertures. In the future, simultaneous amplitude and phase tuning could be achieved with the addition of an amplitude modulator to the device. Figure 1(a) shows a schematic of our Si waveguide fed circular aperture antenna. The Si waveguide is formed on 3 μm of bottom oxide cladding with the waveguide dimensions nominally $w = 400$ nm $\times h = 240$ nm. The metallic antenna aperture is embedded in a capping oxide of thickness, $t \approx 600$ nm, and displaced above the Si waveguide bus by $d \approx 150 - 250$ nm. The metallic antennas are placed in close proximity to the evanescent coupling region of the dielectric waveguides. This couples the optical field of the waveguide into the antenna and produces the radiation from the antenna. Many different antenna designs and feed mechanisms have been fabricated and examined. In the following, we will focus on the linear 1×8 circular aperture antenna array with integrated thermo-optic phase shifters shown in Fig. 1(b). This simple aperture antenna illustrates the basic building block of our phased array; a linear periodic array of emitting aperture antenna with individual phase control integrated into the waveguide feed. The aperture radius is seen to vary with distance along the length of the array to create a uniform emitted power. Here the radius is varied from 500 nm to 750 nm along the feed direction. The antenna aperture is not subwavelength and the emission pattern is not that of an isotropic point radiator. This is mainly due to limitations in the resolution of our deep-UV lithographic patterning step and can be overcome with e-beam patterning. Figs.1 (c)-(d) show the fabricated waveguide arrays emitting surface normally. The far-field radiation pattern is a result of the interference from each aperture emitter in the array similar to diffraction from an array of apertures. The apertures act as secondary sources and the far-field radiation pattern from such an array is directly related to the Fourier transform of the transmitted field amplitude and phase on the emitting apertures.

To model the aperture antenna array, we use vector Smythe-Kirchoff diffraction theory [16] to describe the far-field radiation pattern. Vector diffraction theory relates the transverse electric field in the plane of the apertures to the field at any distance in the scattering region and is given by,

$$\vec{E}(\vec{x}) = \frac{1}{2\pi} \nabla \times \int_A d\vec{r}' \frac{\exp(ik|\vec{x} - \vec{x}'|)}{|\vec{x} - \vec{x}'|} (\hat{e}_z \times \vec{E}_i(\vec{x}')) \tag{1}$$

where the integration is over the transverse electric field ($\vec{E}_i$) in the apertures of the array, and $\hat{e}_z$ is a unit vector normal to the aperture plane. In the far-field, the diffraction integral Eq. (1) simplifies to an outgoing spherical wave front with complex scattering amplitude given by

$$\vec{E}(\vec{x}) \approx \frac{\exp(ikR)}{R} \frac{i}{\lambda} \int_A d\vec{r}' \exp(-ik\hat{x} \cdot \vec{r}')(\hat{x} \times (\hat{e}_z \times \vec{E}_i(\vec{x}'))) = \frac{\exp(ikR)}{R} \vec{F}(\hat{x}), \tag{2}$$

where in the Kirchoff approximation, the self-consistent field in the aperture is replaced by the incident field. Here, $k = 2\pi/\lambda$ where λ is the free space wavelength. The aperture antenna array is in the x-y plane, and $R = |\vec{x}|$ is the distance and $\hat{x}$ is a unit vector pointing to the far-field observation point from a common origin, and $\vec{F}(\hat{x})$ is the scattering amplitude. Note that the source integration can be extended over the entire plane if we assume that the transverse electric field vanishes on the metal. The far-field scattering amplitude is the term that modulates the outgoing spherical wave in Eq. (2), and is the Fourier transform of the transverse electric field distribution in the array of emitting apertures. The transverse electric field in the apertures can be determined from full finite difference time domain (FDTD) electromagnetic simulation of the waveguide fed antenna array. The exact near-field electromagnetic solution in the antenna apertures can be used to determine the far-field radiation pattern from Eq.(2).

While the rigorous aperture near-field distributions can provide some insight into the radiation pattern, it is often very useful to obtain a simple model for the far-field radiation pattern. In the vector Kirchoff approximation, we consider a the incident field distribution to be uniform in the emitting aperture antenna and given by

$$\vec{E}_i(\vec{r}') = \sum_n \tau_n(\vec{r} - \vec{r}_n)A_n \exp(i\phi_n)\hat{\varepsilon}_n \tag{3}$$

where $\vec{r}_n$ is the position of the nth antenna in the plane of the apertures. The uniform amplitude, phase and polarization in the nth aperture are A_n, ϕ_n and $\hat{\varepsilon}_n$, respectively, and τ_n is the nth aperture shape function. The model far-field scattered amplitude for the uniform aperture field is

$$\vec{F}(\hat{x}) = \frac{1}{\lambda} \sum_n A_n \exp(-ik\hat{x}\cdot\vec{r}_n + i\phi_n)(\hat{x}\times(\hat{e}_z\times\hat{\varepsilon}_n))\int d\vec{u}\,\tau_n(\vec{u})\exp(-ik\hat{x}\cdot\vec{u}) \tag{4}$$

For an array with uniform aperture size, the far-field scattering amplitude is given by the product of the vector array function, and the Fourier transform of the aperture shape function. The phase and amplitude on each aperture are included in the vector array function and explicit antenna pattern synthesis is evident. Through proper design of the aperture shapes, spacing, and coupling, it is clear that we can tailor the amplitude distribution across the array and shape the far-field radiation pattern. Furthermore, by controlling of the individual phases of the transverse field in the emitting apertures we can angularly steer the radiation pattern or beam.
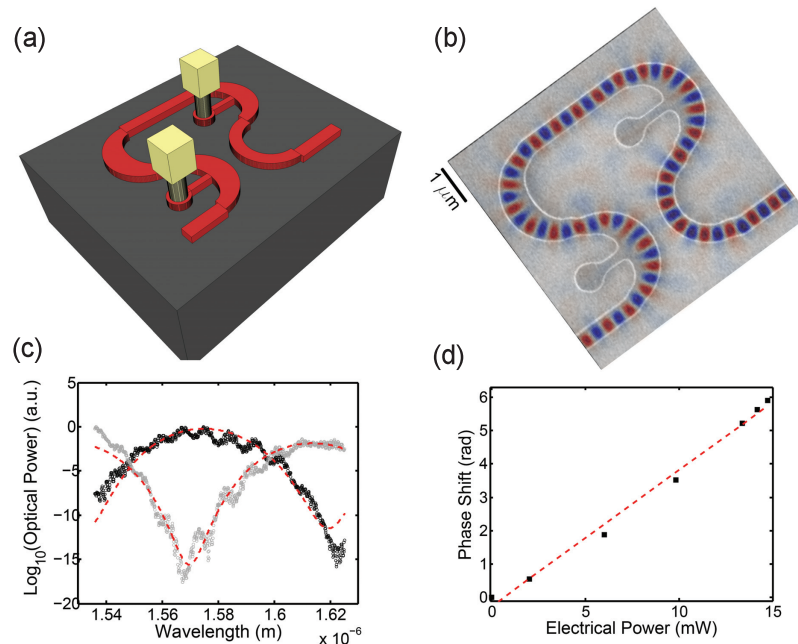

Fig. 2. (a) Schematic of low loss thermo-optic waveguide phase shifter. (b) FDTD waveguide simulation of thermo-optic phase shifter superimposed on SEM image of fabricated device. (c) Mach-Zehnder characterization of the waveguide coupled thermo-optic phase shift showing 0 and π phase shift. (d) Measured phase shift as a function of applied electrical power. The phase shifter length for the 6μm and 9μm phase shifter is $\sim 10\mu$m and $\sim 17\mu$m, respectively.

Electronic phase control is obtained in the waveguide feed and is based on the thermo-optic

effect. The thermo-optic effect creates a change in the index of refraction as a function of temperature and is given by $\Delta n = \alpha \Delta T$, where α is the thermo-optic coefficient. The thermo-optic coefficient for Si at room temperature is quite large [17], $\alpha = 1.8 \times 10^{-4} K^{-1}$, and can be electronically controlled by ohmic heating of doped Si. A schematic of a compact waveguide integrated thermo-optic phase shifters is illustrated in Fig. 2(a). The phase shifter consists of doped Si regions between metal electrodes when a voltage is applied between the metal electrodes the si waveguide is ohmically heated. In order to increase the effective path length, a series of bends were introduced into the phase shifter, furthermore to minimize the scattering loss in the device from the electrical contacts, the center width of the waveguide bends were increased to 0.8 μm from 0.4 μm [18], additionally, offsets were used to reduce modal conversion losses from the straight to bent waveguides. A SEM of the fabricated device along with an overlay of a FDTD simulation is shown in Fig. 2(b). Each phase shifter should be independently capable of phase control. In order to measure the phase shifter tuning under electrical bias, we introduced the device into one arm of an unbalanced Mach Zehnder interferometer which was integrated on-chip. Figure 2(c) shows the measured phase profiles from a 9 μm phase shifter for 0 mW and 10 mW applied electrical power demonstrating π phase shift. From Fig. 2(d), we see that for 15 mW of applied electrical power nearly a 2π phase shift is obtained, therefore individual phase control is possible.

3. Fabrication and experimental setup

A chip-scale platform for phase-steered nanoantenna arrays was developed using 248 nm deep ultraviolet lithography (DUV) in a silicon CMOS foundry. Starting substrates were silicon on insulator (SOI) with 3 μm bottom oxide (BOX) region for bottom cladding and a 13 Ω-cm, 250 nm thick active silicon layer. Silicon waveguides, phase shifters, and splitters were defined using standard lithography and etched using Reactive Ion Etch (RIE). Arsenic, Phosphorous, and Boron implants for active modulators, resisters, and heaters were sequentially done followed by activation and anneals. High density plasma (HDP) CVD oxide was deposited and planarized with chemical mechanical polish (CMP) to a thickness of 200 nm over silicon structures. A Tantalum thin film of 100 nm thickness for nanoantenna definition was deposited via sputter, followed by DUV lithography and RIE etch. Additional HDP CVD oxide was deposited and planarized with CMP to a thickness of 800 nm over silicon waveguides. Contacts were defined and etched. Titanium was used for contact silicide formation via through contact technique of Titanium sputter followed by RTA at 750 °C. Tungsten CVD was used for contact fill and subsequently planarized using CMP. Metal interconnect and pad metal was deposited using a stack of Ti/TiN/AlCu/TiN, followed by definition and etch. Top cladding was deposited using CVD Phosphorsilicate glass with a thickness of 2.5 μm. Aluminum contact pads were defined and etched. Final anneal was 420 °C in forming gas. Combinations of Reactive Ion Etch (RIE) of oxides and deep Bosch etch of silicon substrate were used for silicon waveguide etch facet openings at fiber coupling points. The deep RIE (Bosch) etch was done to a depth of 200 μm to expose the side tapers and provide sufficient room for optical fiber alignment for test.

The integrated aperture antennas and the compact Si waveguide phase-shifter are the key building blocks required for our chip-scale optical phased array. In order to characterize the beam steering performance of our optical phased array in the telecom wavelength band (1500-1600 nm), we constructed a 4-f confocal imaging microscope with accessible pupil plane for far-field Fourier imaging. Our experimental setup is shown in Fig. 3 along with Fourier plane images of the far-field radiation pattern, and the real space images of the emitting antenna array. A lensed fiber from a telecom tunable laser focuses light into a Si waveguide and short wave infrared (SWIR) cameras are used to image simultaneously the surface normal radiation
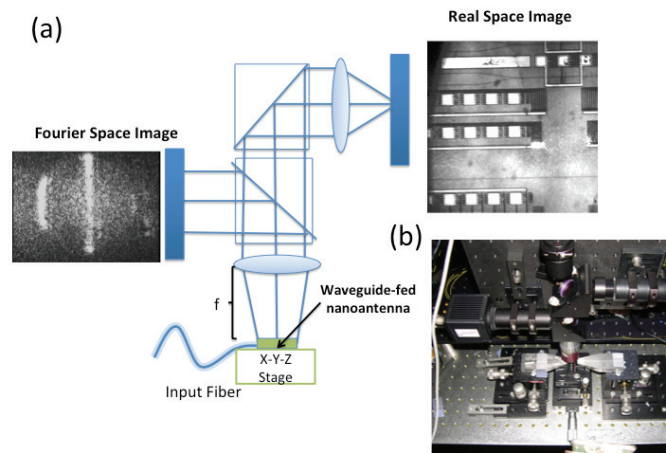
Fig. 3. (a) Schematic of far-field radiation pattern confocal imaging setup with real and Fourier space imaging capability. (b) Image of actual set up with fiber coupling to chip shown.

pattern and the real-space image. A near-IR objective of numerical aperture NA=0.25 (angular cone with half angle $\sim 15°$) was used in collecting all the images obtained.

4. Results

Both 1D and 2D antenna arrays have been fabricated on our test-chip with various aperture shapes and array configurations (see Fig. 1). As previously noted, we will concentrate on a 1×8 linear array of variably sized circular apertures each individually phase-controlled and shown in Fig. 1(b). This array forms the conceptual basis for all of our 2D arrays and can be readily experimentally probed. The sizes of the apertures have been chosen in order to obtain uniform radiated power over the array in a process known as apodization. To create the electronic beam-steering, a set of ganged 1×8 electrical probes with individual power supplies are used to simultaneously bias each phase-shifter, and the far-field radiation pattern is captured on a SWIR camera for the particular applied bias profile. Next, we present the experimental results for 1×8 arrays with pitches of 9 and 6 μm.

The beam-steering characteristics are shown in Fig. 4 for the 9 μm pitch aperture antenna array for fixed wavelength electronic phase scans. The simulated radiation pattern for the linear array is shown in Fig. 4(a) and measured beam-steering angle as a function of applied phase shifter electrical power is shown in Fig. 4(b). An angular steering of the central beam lobe (highlighted in red) of $8°$ degrees has been experimentally demonstrated. The individual snap-shots shown in Figs. 4 (c)-(f) show the grating lobes with the central beam highlighted in red as the applied bias is varied uniformly along the 1×8 linear array.

Figure 5(a) shows the simulated radiation pattern and Fig. 5(b) and the measured electronic phase shift for the 6 μm pitch linear array at fixed wavelength. The measured radiation patterns for various bias steps are shown in Figs. 5(c)-5(f). The beam-steering performance for unifrom bias is shown with the central grating lobe colored red. For the device with a 6 μm pitch, beem steering of $\sim 8°$ has been demonstrated. In both cases as the phase is varied by uniform electrical bias of the individual phase shifters, the central grating lobe emitted surface normally is swept through the Fourier plane of the experimental imaging setup.
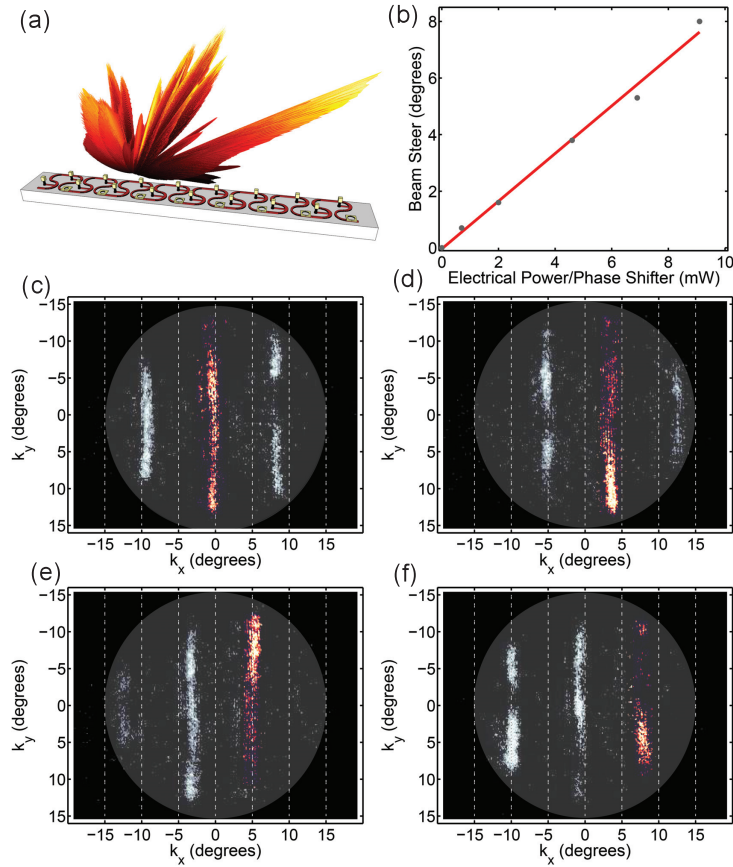
Fig. 4. (a) FDTD simulation of far-field radiation pattern of 1×8 aperture array with 9 μm pitch. (b) Measured angular sweep of central lobe versus applied electrical power for uniform array bias. (c)-(f) Measured surface normal radiation pattern and beam steering characteristics for increasing applied electrical power.

From the simulated radiation pattern, we can estimate the power radiated surface normally. The radiation efficiency is defined as the surface normal radiated power normalized by the incident optical power. The simulated radiation efficiency into a uniform oxide top cladding for the linear array is estimated at $\sim 31\%$. This estimate does not include the refraction losses at the air oxide interface, and can be considerably enhanced with the addition of an optimal ground plane.

The angular spacing between grating lobes in the far-field radiation pattern is governed by the period between adjacent antenna emitters. In Fig. 5, the 6 μm pitch array has grating lobes at the edge of the imaging pupil (angular lobe separation $\sim 14°$) while the 9 μm pitch array in Fig. 4 has lobes in the pupil with lobe separation of $\sim 9°$. This clearly illustrates that it is the period of the emitters that limits the angular scan range before another grating lobe appears. Also present in both aperture arrays, the simulated radiation patterns show significant forward scattering lobes. This results from a non-uniform phase over each aperture and can be attributed to the large aperture size and significant scattering from the metallic edge of each plate, which can be circumvented in the future with higher resolution optical lithography.

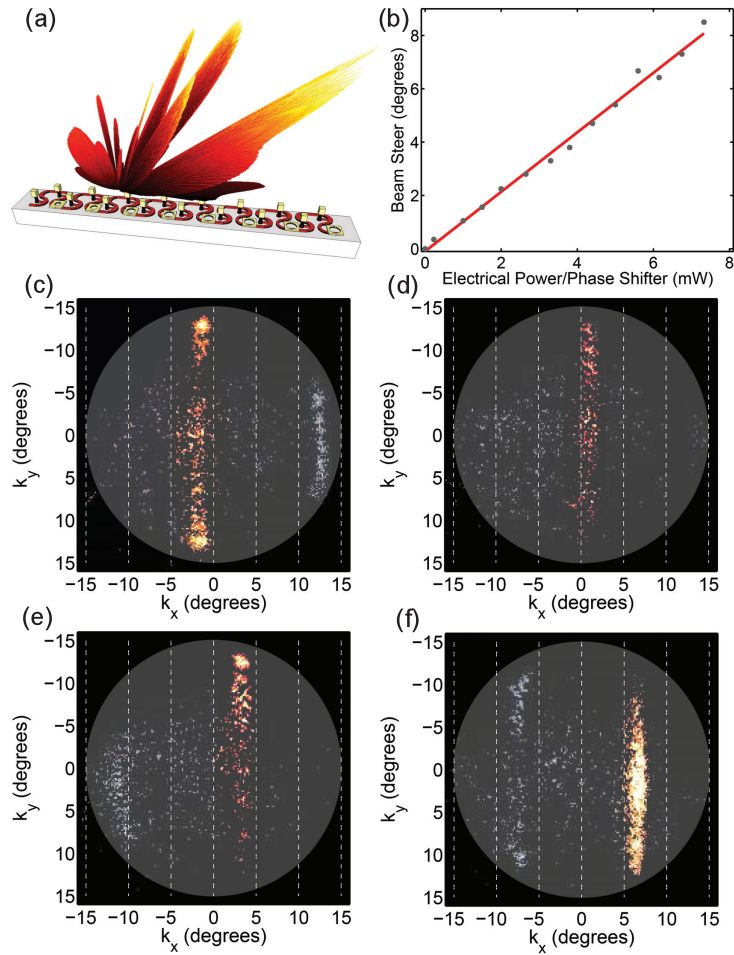Figure 6 shows a comparison of the measured radiation patterns with the Smythe Kirchoff

Fig. 5. (a) FDTD simulation of far-field radiation pattern of 1×8 aperture array with $6\,\mu$m pitch. (b) Measured angular sweep of central lobe versus applied electrical power for uniform array bias. (c)-(f) Measured surface normal radiation pattern and beam steering characteristics for increasing applied bias voltage.
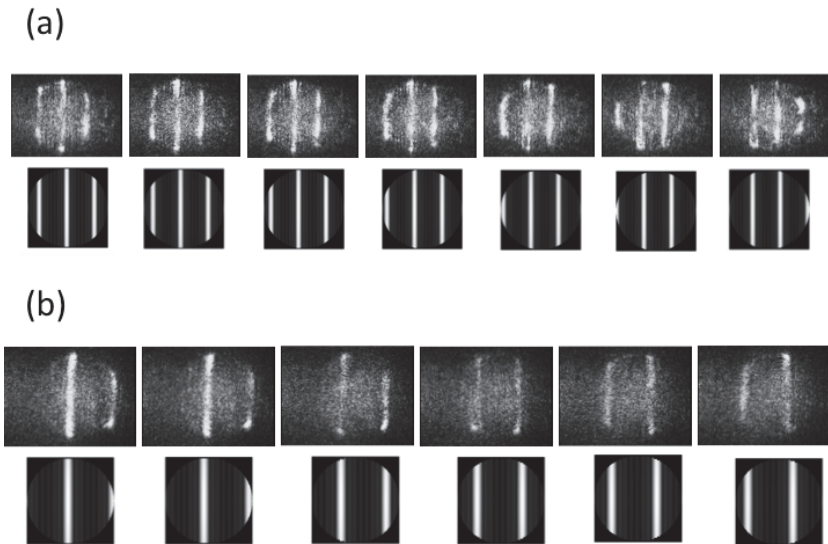
Fig. 6. (a) Measured surface normal radiation pattern and beam steering sweep data for 9 μm pitch aperture antenna array with comparison to the Smythe vector diffraction theory with estimated uniform phase profile at fixed wavelength (Media 1). (b) Measured and theoretical surface normal radiation sweep data for the 6 μm pitch aperture antenna array (Media 2).

(Eq. (2)) predicted radiation patterns for fixed wavelength bias scans for both the 6 and 9 μm periodic arrays. In both cases, it is clear that the central interference fringe is swept out into the secondary fringes although not completely in the 6 μm case. The simulated phase scans for the uniform amplitude circular aperture arrays are shown for comparison. In these simulations, the amplitude was taken to be unity in each aperture ($A_n = 1$ and the phase on the nth aperture is $\phi_n = 2\pi n P \sin(\theta)/\lambda$, where P is the grating pitch, and θ is the maximum steering angle. From simulation amd measurement we estimate an angular beam-width of $1°$ from the full width at half max. From the simulations and measurements, we observe an angular sidelobe seperation of $9°$ and $14°$ for the 9 and 6 μm pitch arrays respectively. Continuous sweeping of the linear array was obtained by applying computer controlled uniform bias to the each phase shifter, Fig. 6(a) and 6(b) show snapshots at approximately 2 mW increments.

5. Conclusion

In conclusion, we have demonstrated electronically controlled beam-steering of a linear array of aperture nanoantennas through an NA=0.25 at fixed wavelength in the telecom band. Electronic angular beam steering of $8°$ was demonstrated for a 1×8 optical nanonantenna phased array. Angular side-lobe seperations of $14°$ and $9°$ for the 6 and 9 μm period arrays have been observed. The measured beam-width of $1°$ for the linear 1×8 antenna array can be further improved by increasing the number of the emitting antenna in the phased array. The optical phased array of nanoantenna have been fabricated in a CMOS compatible Si photonic process allowing for chip-scale integration with control electronics, and potential integration with advanced Ge detectors [19] for receiver applications. Si photonic waveguide thermo-optic phase-shifters have been integrated to control the phase of each emitting nanoantenna element, and have

demonstrated $\sim 2\pi$ phase-shift under electrical bias. While the integrated waveguide phase-shifters are compact, they do limit the antenna spacing and hence the angular steering range. The angular beam-steering range can be greatly extended by decreasing the period between the emitting elements to sub-wavelength dimensions at the cost of giving up individual control over the phase of each emitter. This suggests that sub-wavelength dense antenna arrays capable of large angle sweeping with electronic control can be maintained by thermo-optic tuning of larger linear blocks. The radiation efficiency of the antenna array can be improved by incorporating an optimized ground plane. Substantial improvement in radiation efficiency has been seen with nitride waveguide fed antenna above an optimized ground plane reflector. It is also possible to remove forward scattered lobe by using a continuous thin metallic template and reducing the size of the emitting aperture. This approach requires e-beam lithography patterning for antenna definition. These preliminary beam-steering results suggest a method for decreasing the antenna period to sub-wavelength dimensions, and simulations indicate that steering through $\pm 45°$ or more is possible. In the large angle case, aperture shaping and apodization can be fully utilized to reduce the grating lobes in the array function.

Acknowledgments